International Journal of Microwave and Wireless Technologies

cambridge.org/mrf

Improved model for microstrip antennas loaded by metallic vias with lumped elements

Fúlvio F. Oliveira[1], Juner M. Vieira[2], Daniel B. Ferreira[1] and Daniel C. Nascimento[1]

[1]Laboratory of Antennas and Propagation, Aeronautics Institute of Technology, São José dos Campos, SP, Brazil and [2]Division of Space Electronics and Computing, National Institute for Space Research, São José dos Campos, SP, Brazil

Research Paper

Cite this article: Oliveira FF, Vieira JM, Ferreira DB, Nascimento DC (2025) Improved model for microstrip antennas loaded by metallic vias with lumped elements. *International Journal of Microwave and Wireless Technologies* **17**(1), 140–148. https://doi.org/10.1017/S1759078725000261

Received: 7 October 2024
Revised: 14 February 2025
Accepted: 17 February 2025

Keywords:
Microstrip antennas; multiband antennas; reconfigurable antennas; resonant cavity model; varactor diodes

Corresponding author: Juner M. Vieira; Email: juner.vieira@inpe.br

Abstract

This letter presents an improved analytical model for analyzing probe-fed microstrip antennas loaded by metallic vias with lumped terminations. The proposed formulation is based on the resonant cavity model and enables efficient analysis of such perturbed radiators for various types of terminations. The model is validated through the analysis of two antennas: one operating in a TM_{00} mode and the other with four capacitive terminations to produce circular polarization. Moreover, a reconfigurable RHCP/LHCP antenna based on the patch with capacitive terminations has been manufactured and tested, showing a broadside axial ratio below 0.5 dB at 1.575 GHz.

Introduction

Microstrip antennas loaded by metallic vias have been widely employed in the antennas and propagation scientific community for several decades [1, 2] and continue to be the subject of recent studies [3–6]. Embedded metallic vias offer versatility in antenna design and find applications in various contexts. Reconfigurable Antennas: In this group, tunable components such as varactors [4, 5, 7] and p-i-n diodes [2, 6, 8] are connected to the patch through metallic vias, enabling adjustments of the antenna parameters. Perturbations: Metallic vias are employed to change the characteristics of patch antennas, achieving multiband operation and modified radiation patterns [9–12]. Substrate Integrated Waveguide: Shorting pins are employed to realize electric walls, enabling the development of compact radiators with enhanced performance [13–15]. Small Antennas: The combination of shorting pins and reactive terminations is effective in reducing the radiator dimensions [5, 10].

The analysis of microstrip antennas loaded by metallic pins traditionally relies on computationally intensive full-wave simulations, which require significant processing and memory resources. In this context, there is a growing interest in employing fast analytical techniques to provide designers with initial geometries and performance estimates before using full-wave tools [12, 16, 17].

This letter introduces an improved analytical method for analyzing rectangular microstrip antennas loaded by metallic vias with lumped terminations. The formulation is based on the analysis of an *n*-port resonant cavity [17] by means of the eigenfunction expansion method. It is worth noting that [17] has primarily focused on computing resonant frequencies and input impedance of linearly polarized (LP) patches. In contrast, our work emphasizes a model capable of computing radiation patterns and enabling multimode operation, including circularly polarized (CP) patches. This approach offers a low computational cost and good accuracy, making it a valuable predesign tool for estimating initial geometry and antenna performance. Moreover, it provides designers with physical insights into the radiator's operation.

The novelties of this letter are as follows:

(i) *A Strategy for the Radiated Far-Field Computation*: The proposed model incorporates the superposition of non-resonant modes to represent the field of a perturbed cavity. This technique allows, for example, comprehensive analysis of the radiated fields of antennas operating in TM_{00} mode [11, 12] and simplifies the examination of circular polarization in perturbed antennas [1].

(ii) *Multiband Operation Analysis*: The model offers insights into the performance of multiband antennas [18], through the effects of non-resonant modes on input impedance.

(iii) *Application in Reconfigurable Antenna*: The proposed method is a useful tool for the predesign of reconfigurable patch antennas [19, 20], providing robust support for future advancements in this area.

This letter begins by detailing the formulation of the *P*-port cavity model. Afterward, the designs of CP and LP antennas are demonstrated and compared with results obtained

© The Author(s), 2025. Published by Cambridge University Press in association with The European Microwave Association.

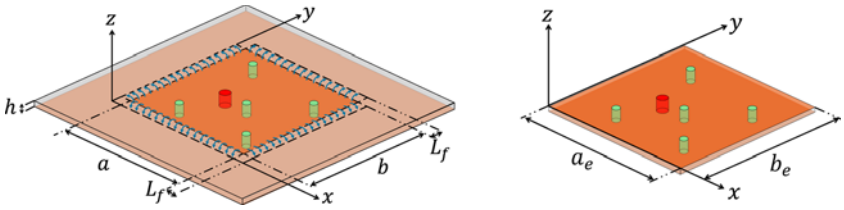


Figure 1. Microstrip antenna loaded by metallic vias. (a) Proposed geometry. (b) Equivalent resonant cavity.

from HFSS software. Finally, to further validate the model, a prototype of a polarization reconfigurable antenna is manufactured and tested.

Antenna modeling

The proposed antenna geometry, depicted in fig. 1(a), is based on the canonical rectangular form ($a \times b$) printed on a low-loss substrate of thickness h. The radiator includes a ground plane and a set of metallic pins positioned vertically within the substrate. These pins can be used to connect the patch either to the ground plane or to grounded components such as inductors, capacitors, varicaps, or p-i-n diodes. The antenna is fed by a coaxial probe, illustrated as the red pin. Consistently, the fringing fields are represented in the geometry with a length L_f at the edges of the patch [21].

In this work, the antenna is modeled by an equivalent resonant cavity [22], as illustrated in fig. 1(b). The cavity, with dimensions $a_e \times b_e$, where $a_e = a + 2L_f$ and $b_e = b + 2L_f$, consists of two electric walls (patch and ground plane) and four magnetic walls around the periphery. The feed probe and the metallic pins are modeled as strips with uniform electric current densities $\vec{J}_{fp}$. In this way, the problem can be interpreted as a P-source cavity or equivalently a P-port circuit.

The analysis of the antenna is divided into three main parts: (a) computing the electromagnetic field inside the cavity; (b) evaluating the far field; and (c) determining the input impedance.

Electric field in the equivalent cavity

For electrically thin antennas, i.e., those whose thickness h is significantly smaller than the wavelength λ in the substrate, the electric field in the equivalent cavity exhibits only the E_z component, which can be written using modal expansion as [22]

$$E_z(x,y) = \sum_{m=0}^{\infty}\sum_{n=0}^{\infty} E_{mn}\Psi_{mn}(x,y), \tag{1}$$

where E_{mn} is the amplitude of each TM^z_{mn} mode and $\Psi_{mn}(x,y) = \cos(m\pi x/a_e)\cos(n\pi y/b_e)$.

The amplitude E_{mn} is computed from the solution to the non-homogeneous wave equation $(\nabla^2 + k^2)E_z = j\omega\mu_0\vec{J}_f \cdot \hat{z}$:

$$E_{mn} = \frac{j\omega\mu_0 \iint_S J_f \Psi^*_{mn}(x,y)\, ds}{(k^2 - k^2_{mn})\iint_S |\Psi_{mn}(x,y)|^2 ds}, \tag{2}$$

where S denotes the cavity surface located in the xy-plane, $\vec{J}_f$ is the total current density comprised of P sources representing the feed probe and metallic pins, $k_{mn} = \sqrt{(m\pi/a_e)^2 + (n\pi/b_e)^2}$ is the resonant wavenumber, and $k = \omega\sqrt{\mu_0\varepsilon_r\varepsilon_0}$ is the wavenumber in a lossless cavity.

The pth source of current density amplitude J_{0p} ($1 \leqslant p \leqslant P$) is modeled as a strip with width L_p [23] and height h, centered at the coordinates (x_p, y_p). Therefore, the total current density $\vec{J}_f$ is given by

$$\vec{J}_f(x,y) = \sum_{p=1}^{P} J_{fp}(x,y)\,\hat{z} = \sum_{p=1}^{P} J_p(y)\,\delta(x - x_p)\,\hat{z}, \tag{3}$$

where

$$J_p(y) = \begin{cases} J_{0p}, \text{ if } |y - y_p| \leqslant L_p/2 \\ 0, \text{ elsewhere} \end{cases}. \tag{4}$$

After substituting (3) into (2) and evaluating the double integrals, the amplitude of each mode is written as

$$E_{mn} = \frac{j\omega\mu_0}{a_e b_e}\frac{\xi_m\xi_n \sum_{p=1}^{P} J_{0p}L_p\Psi_p}{k^2 - k^2_{mn}}, \tag{5}$$

where $\Psi_p = \cos(m\pi x_p/a_e)\cos(n\pi y_p/b_e)\,\mathrm{sinc}(n\pi L_p/2b_e)$, with $\xi_\tau = 1$, if $\tau = 0$, and $\xi_\tau = 2$, otherwise, and $\mathrm{sinc}(x) = \sin(x)/x$.

Finally, applying (5) in (1), the electric field inside the cavity is established as a function of the current densities J_{fp}.

Far field

Using the magnetic surface currents on the magnetic walls of the equivalent cavity, the far-zone radiated field by the microstrip antenna can be computed by applying the Equivalence Principle and the electric vector potential [24]. The expressions for the far-field components $E_{\theta_{mn}}(\theta,\phi)$ and $E_{\phi_{mn}}(\theta,\phi)$ for the TM^z_{mn} modes are well-established in the literature [25, 26] and are not detailed here.

The radiation pattern of a canonical rectangular microstrip antenna is often well characterized by the TM^z_{01} or TM^z_{10} modes in LP designs. In contrast, for CP radiators, the superposition of these two modes adequately represents the far field. However, in this work, due to the multiple sources within the cavity, a strong dependence on several modes to describe the E_z field, as given by (1), is observed. As a result, the far field can be accurately described only if the radiated fields by each TM^z_{mn} mode are superimposed. Thus,

$$E_\theta(\theta,\phi) = \sum_{m=0}^{\infty}\sum_{n=0}^{\infty} E_{\theta_{mn}}(\theta,\phi), \tag{6}$$

$$E_\phi(\theta,\phi) = \sum_{m=0}^{\infty}\sum_{n=0}^{\infty} E_{\phi_{mn}}(\theta,\phi), \tag{7}$$

https://doi.org/10.1017/S1759078725000261 Published online by Cambridge University Press

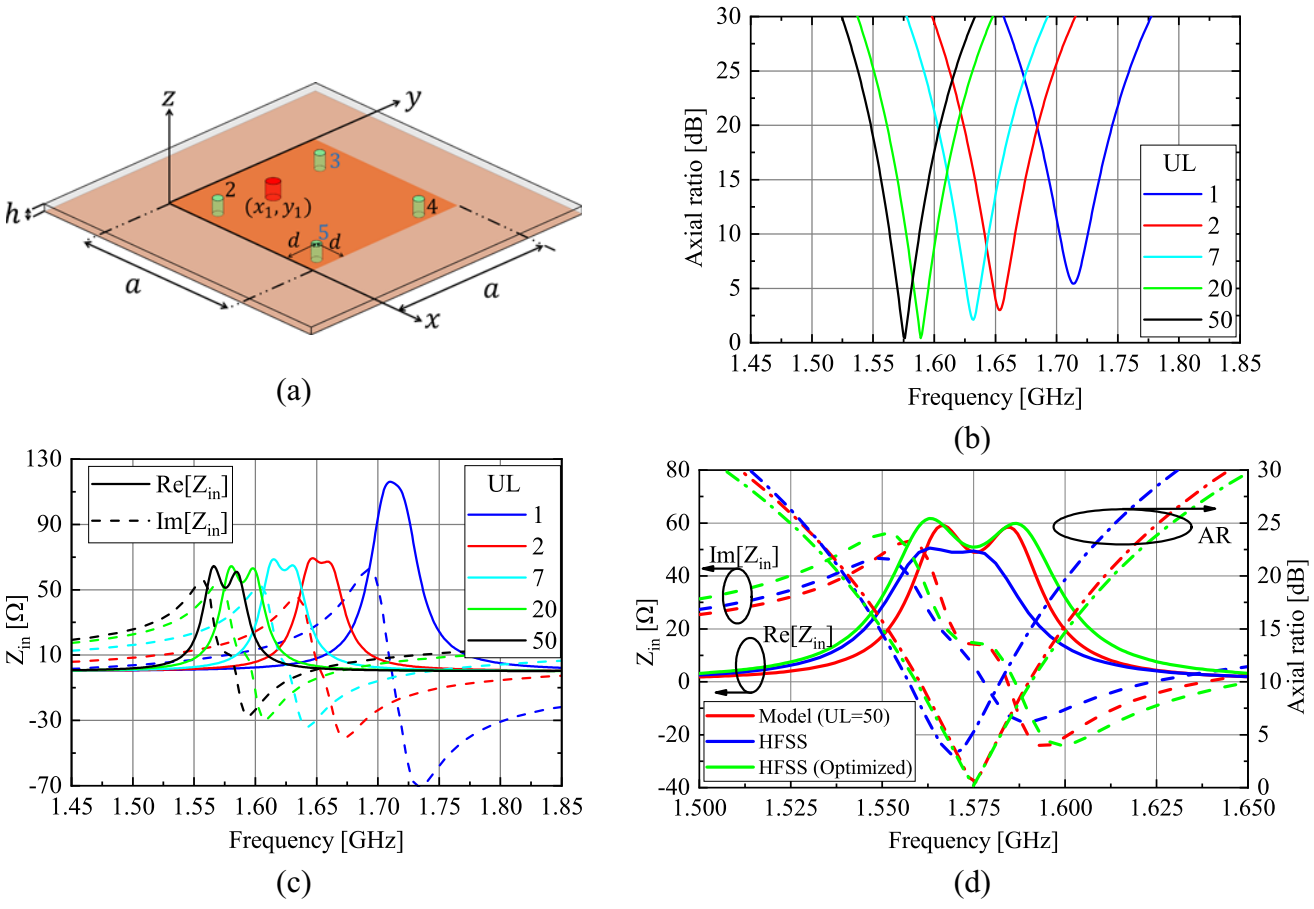


Figure 2. CP antenna loaded by capacitors. (a) Geometry. (b) Axial ratio. (c) Input impedance. (d) Comparisons with HFSS.

The dependency on the number of modes to describe the radiated fields (6) and (7), as well as the input impedance will be further explored in Section III–A.

Input impedance

The complex power delivered by the pth source to the cavity can be calculated using the complex Poynting's theorem as $P_{in_p} = -\frac{1}{2}\int\int\int_V E_z J_{fp}^* dv$. Hence, the total complex power delivered to the cavity is obtained by summing the powers delivered by all sources. According to the circuit theory, the power supplied by the pth source is $P_{in_p} = \frac{1}{2} Z_{in_p} \left|I_{in_p}\right|^2$, leading to the input impedance of the pth port:

$$Z_{in_p} = -\frac{1}{\left|I_{in_p}\right|^2} \int\int\int_V E_z J_{fp}^* dv, \tag{8}$$

where $I_{in_p} = J_{0p} L_p$ is the complex current on the pth source.

Substituting (1) and (5) into (8) and evaluating the triple integral yields the input impedance of the pth port:

$$Z_{in_p} = \frac{-j\omega\mu_0 h}{a_e b_e} \sum_{q=1}^{P} \frac{I_{in_q}}{I_{in_p}} \sum_{m=0}^{\infty} \sum_{n=0}^{\infty} \frac{\xi_m \xi_n \Psi_p^2}{k^2 - k_{mn}^2}. \tag{9}$$

Modeling the cavity as a P-port linear circuit, represented by a $[Z]$ matrix of elements Z_{pq}, the voltage on the pth port is given by $V_{in_p} = \sum_{q=1}^{P} Z_{pq} I_{in_q}$. Then, the input impedance of the pth port is $Z_{in_p} = \sum_{q=1}^{P} Z_{pq} I_{in_q} / I_{in_p}$. This leads to the following expression for the element Z_{pq}:

$$Z_{pq} = \frac{-j\omega\mu_0 h}{a_e b_e} \sum_{m=0}^{\infty} \sum_{n=0}^{\infty} \frac{\xi_m \xi_n \Psi_p^2}{k^2 - k_{mn}^2}. \tag{10}$$

Up to this point, we have assumed that the antenna has P ports. We impose that port 1 corresponds to the feed probe, while the others are terminated with loads Z_{L_q}, and without loss of generality, assuming $I_{in_1} = 1$ A, the following linear system is found:

$$\begin{bmatrix} Z_{22} + Z_{L_2} & Z_{23} & \dots & Z_{2P} \\ Z_{32} & Z_{33} + Z_{L_3} & \dots & Z_{3P} \\ \vdots & \vdots & \ddots & \vdots \\ Z_{P2} & Z_{P3} & \dots & Z_{PP} + Z_{L_P} \end{bmatrix} \cdot \begin{bmatrix} I_{in_2} \\ I_{in_3} \\ \vdots \\ I_{in_P} \end{bmatrix} = \begin{bmatrix} -Z_{21} \\ -Z_{31} \\ \vdots \\ -Z_{P1} \end{bmatrix}. \tag{11}$$

The currents I_{in_q} are determined by solving (11), and consequently, the antenna input impedance is calculated as $Z_{in_1} = \sum_{q=1}^{P} Z_{1q} I_{in_q}$. These currents play a crucial role in computing

https://doi.org/10.1017/S1759078725000261 Published online by Cambridge University Press

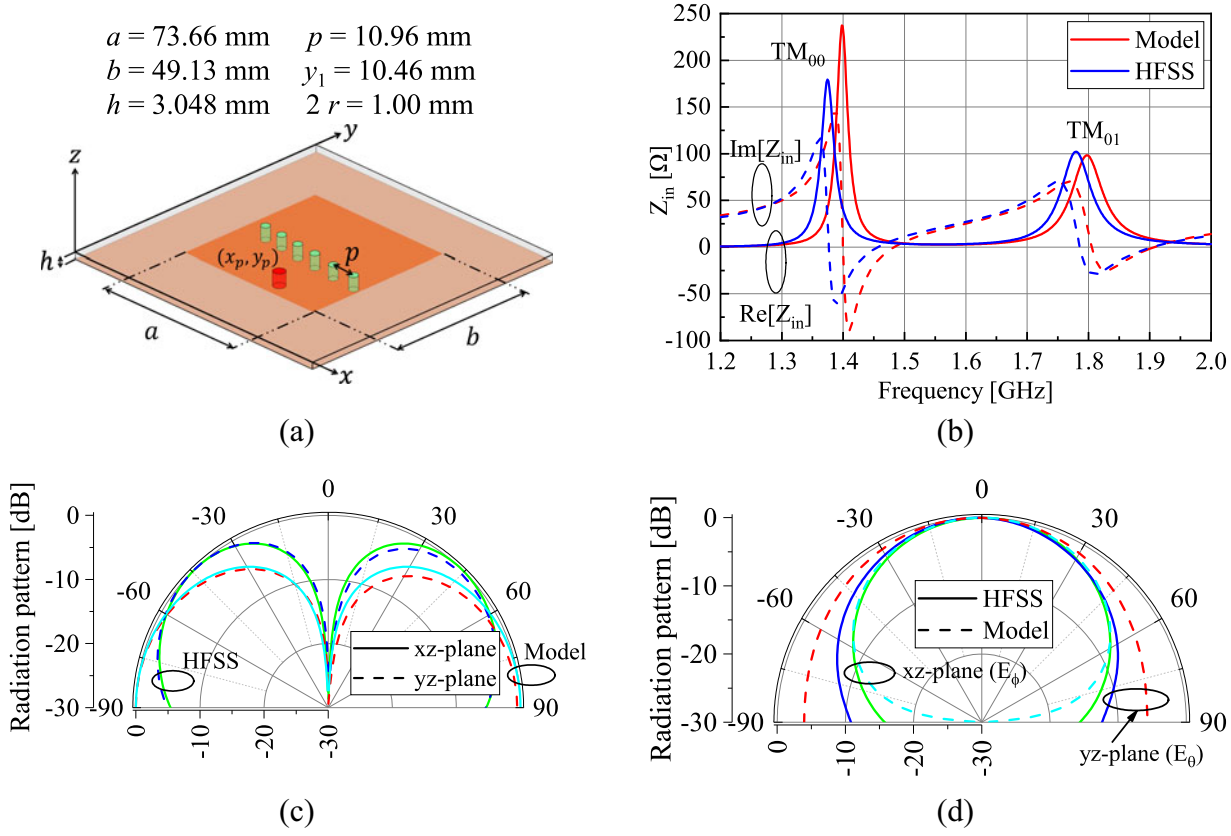


Figure 3. Dual mode antenna loaded by metallic vias. (a) Geometry. (b) Input impedance. (c) Radiation pattern TM^z_{00}. (d) Radiation pattern TM^z_{01}.

(5) and subsequently in determining the far field described in (6) and (7).

Effective loss tangent

The effects of radiated power P_i, metallic loss P_c, and dielectric loss P_d are computed and incorporated into the model using the effective loss tangent concept [22]. This parameter is calculated for each TM^z_{mn} mode as $\delta_{ef\,mn} = (P_i + P_c + P_d) / (2\omega_{mn} W_{e_{mn}})$, where ω_{mn} is the angular resonant frequency given by $\omega_{mn} = c_0 k_{mn}/\sqrt{\varepsilon_r}$, and $W_{e_{mn}}$ represents the stored electric energy in the cavity for each mode. Therefore, the effective wavenumber of each mode is computed as $k_{ef\,mn} = k\left(1 - j\,\delta_{ef\,mn}\right)^{1/2}$, which replaces k in (2), (5), (9), and (10), properly incorporating the losses into the model. The surface wave loss is ignored in $\delta_{ef\,mn}$ due to its negligible effect on electrically thin antennas [24].

The challenge of computing $\delta_{ef\,00}$ of the TM^z_{00} mode is a known issue in the literature [23], which seems not clearly solved yet. In this study, we address this challenge by employing the following rule: $\delta_{ef\,00} = \delta_{ef\,10}$, if $a_e > b_e$, or $\delta_{ef\,00} = \delta_{ef\,01}$, if $a_e < b_e$. The accuracy of this choice is demonstrated in the next section. Furthermore, the computation of $\delta_{ef\,mn}$ is conducted for the unloaded antenna, similar to a classical rectangular microstrip patch [24].

Validation of the proposed model and case study

To validate the proposed model, we analyze two antennas: one with grounded capacitors and the other with shorted metallic vias. We compare the results obtained from our model with those generated by the HFSS simulator.

Circularly polarized antenna

Initially, we analyze the CP antenna illustrated in fig. 2(a). It consists of a square patch with a side length $a = 37.19$ mm ($a_e = 40.25$ mm) and a 50 Ω probe positioned at $x_1 = 11.3$ mm and $y_1 = a/2$. Four metallic pins with a radius of 0.5 mm are placed at a distance $d = 2.0$ mm from the antenna corners, connecting grounded capacitors to the patch. The antenna is printed on a laminate with a thickness of 3.048 mm, characterized by a relative permittivity $\varepsilon_r = 2.55$ and loss tangent $\tan\delta = 0.002$. For proper CP operation at 1.575 GHz, the capacitances, acting as perturbations in the cavity, are tuned as follows: capacitances $C_1 = 1.346$ pF are connected in vias 2 and 4, resulting in $Z_{L2} = Z_{L4} = -j75\ \Omega$. Similarly, capacitances $C_2 = 1.296$ pF are connected in vias 3 and 5, leading to $Z_{L3} = Z_{L5} = -j78\ \Omega$.

These values were obtained through the following systematic procedure. First, all four capacitances were initially set to 1.3 pF, providing an intermediate capacitive reactance within the range offered by the chosen varicap BB833 from Infineon Technologies. Next, the equivalent side length a_e was adjusted to achieve a resonance close to the target operating frequency of 1.575 GHz, resulting in a LP antenna at this stage. Finally, a parametric study was conducted to determine the values of C_1 and C_2. This analysis involved slight variations to the initial capacitances, allowing for the optimization of the antenna's circular polarization performance.

The choice of the upper limit (UL) for the indexes m and n in the summations is crucial for the performance of the proposed model.

https://doi.org/10.1017/S1759078725000261 Published online by Cambridge University Press

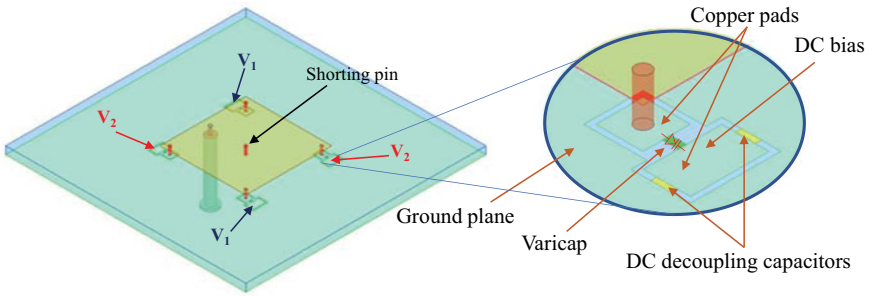


Figure 4. Geometry of the reconfigurable antenna.

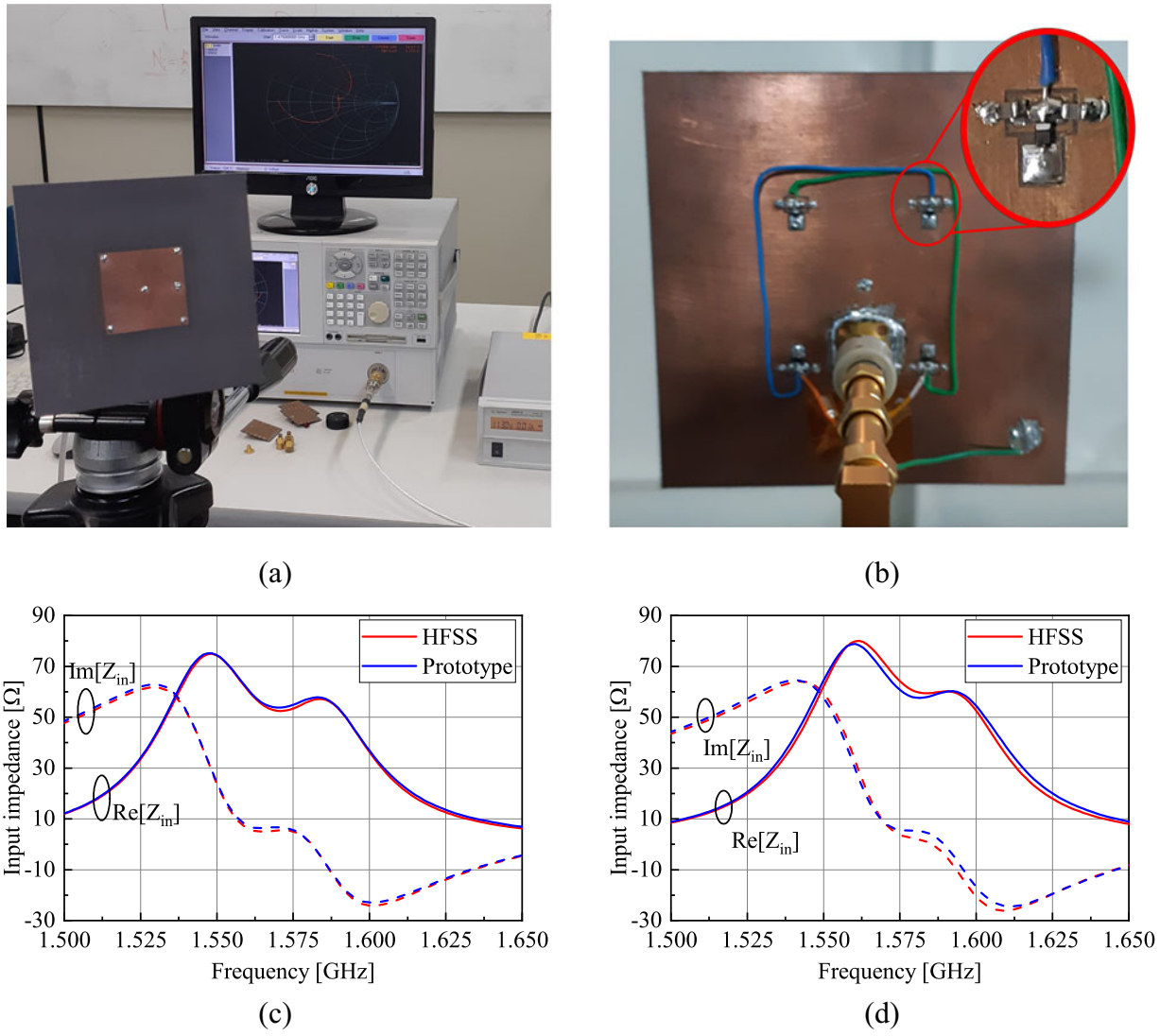


Figure 5. Prototype. (a) Front view and input impedance measurement setup. (b) Back view. (c) Input impedance (RHCP state). (d) Input impedance (LHCP state).

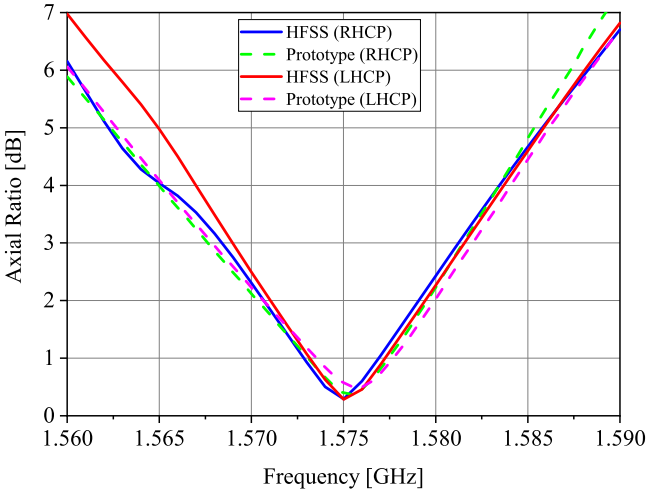
This aspect is examined by computing the input impedance of the proposed antenna. Assuming the same *UL* for both *m* and *n*, we calculate the broadside axial ratio (AR) [27] and input impedance for different values of *UL*, as shown in fig. 2(b) and (c), respectively. Initially, with $UL = 1$, a resonance at approximately 2.3 GHz would be expected for the unloaded cavity. However, due to the capacitive loading of the vias and the coupling of the modes, the antenna resonates at nearly 1.71 GHz (blue curves in fig. 2(c)). When *UL* tends to 50, both the input impedance and AR converge (black curves) and exhibit the performance of a CP antenna. This analysis suggests that the two resonant modes depicted by the black curves in fig. 2(c) are strongly influenced by the modes of the unloaded cavity that resonate away from the operating frequency.

To validate our analysis, we simulated the antenna using HFSS. The comparison, illustrated in fig. 2(d), demonstrates a close agreement for both input impedance and broadside axial ratio. Next, tuning the capacitances and the probe position in HFSS ($C_1 = 1.405$ pF, $C_2 = 1.325$ pF, and $x_1 = 9.5$ mm), the results

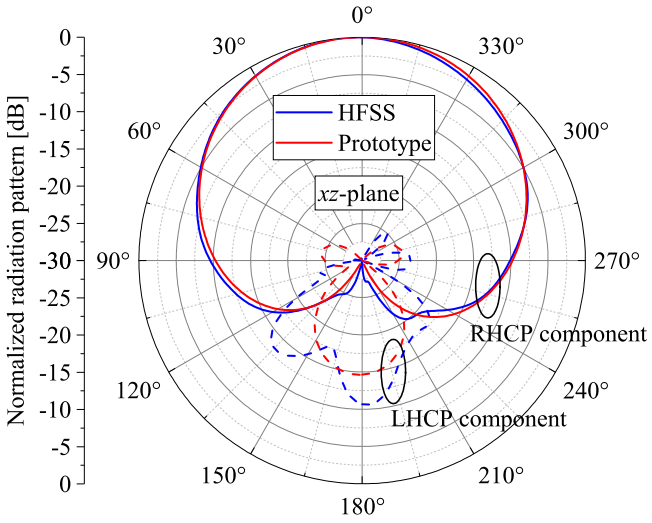
https://doi.org/10.1017/S1759078725000261 Published online by Cambridge University Press



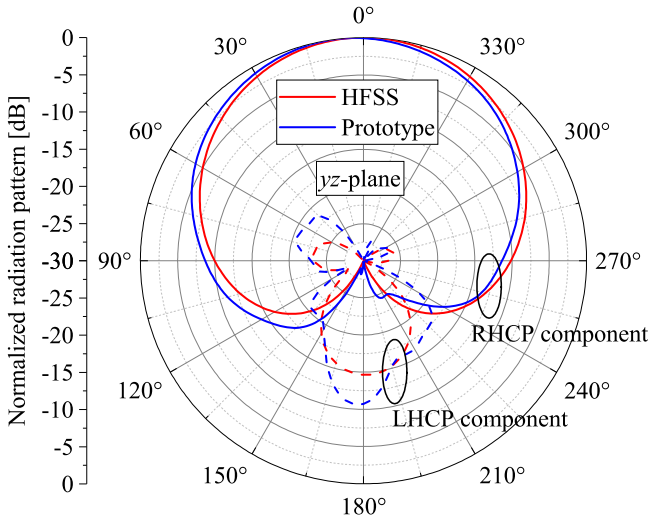
(a)



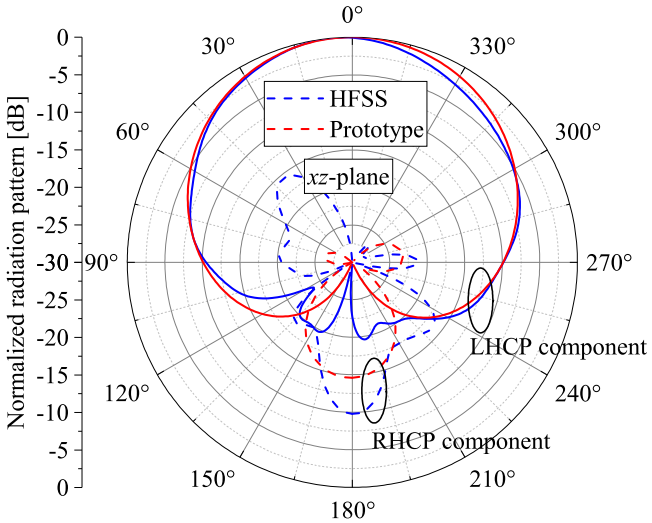
(b)



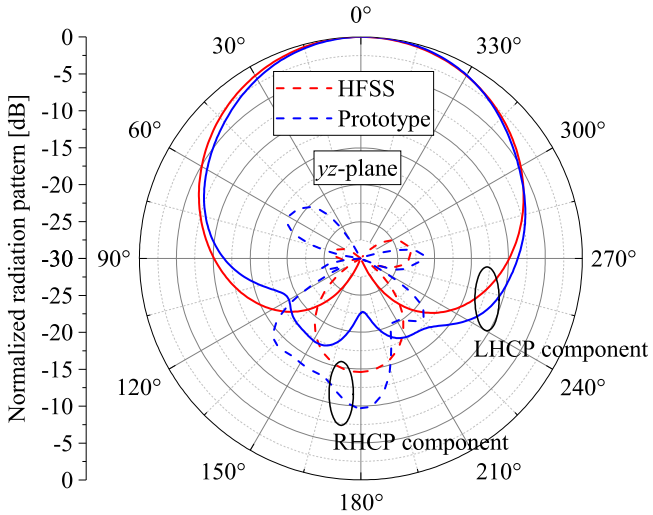
(c)



(d)



(e)



(f)

Figure 6. Prototype radiation patterns. (a) Measurement setup. (b) Broadside axial ratio. (c) *xz*-plane (RHCP state). (d) *yz*-plane (RHCP state). (e) *xz*-plane (LHCP state). (f) *yz*-plane (LHCP state).

https://doi.org/10.1017/S1759078725000261 Published online by Cambridge University Press

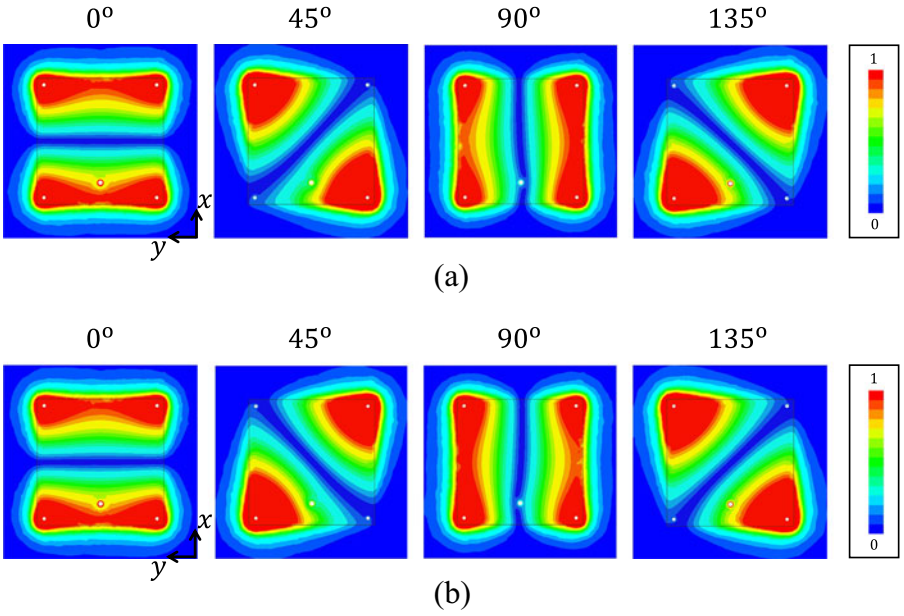


Figure 7. Normalized magnitude of the electric field within the dielectric substrate. (a) RHCP configuration. (b) LHCP configuration.

closely matched those obtained from the cavity model. The updated load impedances are $Z_{L2} = Z_{L4} = —j72\ \Omega$ and $Z_{L3} = Z_{L5} = —j76\ \Omega$. Note that only minor adjustments were necessary to achieve the final geometry, highlighting the potential of the model as a predesign tool.

Antenna operating in the TM_{00} mode

The antenna operating in the TM_{00}^z mode is a well-known radiator based on shorting pins, renowned for its monopole-like radiation pattern [9, 10]. To evaluate the effectiveness of our formulation, we analyzed the antenna depicted in fig. 3(a) and assumed $UL = 50$ in the sums. Following the methodology described in [11], the radiator is designed for dual-band resonance. The lower band is governed by the TM_{00}^z mode, with a resonant frequency close to 1.4 GHz, while the upper band is controlled by the TM_{01}^z mode, close to 1.8 GHz. The design is conducted using the microwave laminate mentioned earlier, and the final dimensions are listed in fig. 3(a). Comparisons with HFSS for input impedance versus frequency and the radiation pattern in both bands are presented in fig. 3(b), (c), and (d), demonstrating good agreement. The slight deviation in the resonant mode at 1.4 GHz may be attributed to challenges in characterizing the loss tangent of the TM_{00}^z mode, as mentioned above.

According to our formulation, the resonance at 1.4 GHz is strongly influenced by neighboring resonant modes, suggesting a perturbed mode with an E_z field distribution similar to Ψ_{00}. Hence, this resonance was classified as TM_{00}^z. It is important to note that there is no resonant frequency associated with k_{00}. Moreover, as the pins are positioned along the region of the null of Ψ_{01}, the resonance at 1.8 GHz remains unaffected by the presence of the pins and is controlled by the unloaded TM_{01}^z mode.

Prototype

The final stage of validating the analytical model involves constructing a reconfigurable CP antenna operating at 1.575 GHz (GPS L1 band). This antenna, based on the geometry presented in Section III–A, is designed to switch between RHCP and LHCP, which is useful for GNSS reflectometry [28]. Reconfigurability is achieved using four varicap diodes BB833 to synthesize the loads Z_{Lp}.

The antenna is printed on the same substrate as the previous designs, and its initial dimensions are derived from the cavity model: $a = 37.25$ mm, $x_1 = 6.40$ mm, and $y_1 = a/2$, with metallic vias of radius 0.5 mm. The varicap cathode is soldered onto a floating copper pad, which is connected to the ground plane through two 1000 pF decoupling capacitors, as illustrated in fig. 4. Consequently, for RF signals, the varicap cathode is directly connected to the ground through a low-reactance path, while it is isolated from the ground for DC voltages. Additionally, a shorting pin with a radius of 0.5 mm is placed at the center of the patch to allow the connection of the varicap anode to the ground for DC voltages. The varicap bias voltage is then applied between the floating copper pad and the ground. It is important to note that this shorting pin does not disturb the electric field distribution under the patch, as the field is null at the center position. A similar biasing solution was used in the reconfigurable filter presented in [29], which eliminates the need for an RF choke to isolate the DC source. Subsequently, the radiator dimensions and the positioning of the varicaps were optimized in HFSS to account for the bias elements introduced in the geometry, resulting in the following dimensions: $a = 34.00$ mm and $x_1 = 3.00$ mm.

The front and back views of the antenna prototype, along with the input impedance measurement setup, are shown in fig. 5(a) and (b). By experimentally adjusting the bias voltages to $V_1 = 12.45$ V and $V_2 = 11.45$ V, the antenna operates in the RHCP state, while reversing these voltages produces the LHCP state. The measured input impedances for both RHCP and LHCP states are presented in fig. 5(c) and (d), respectively. The radiation patterns were measured using an MVG StarLab system, as depicted in fig. 6(a). The broadside AR versus frequency is illustrated in fig. 6(b), showing levels below 0.5 dB for both RHCP and LHCP states at 1.575 GHz. fig. 6(c) and (d) present the normalized radiation patterns for the RHCP state, including the co-pol and cross-pol components in the principal planes (*xz* and *yz*) at 1.575 GHz. Similarly, fig. 6(e) and (f) show the normalized radiation patterns for the LHCP state, highlighting the co-pol and cross-pol components. From

https://doi.org/10.1017/S1759078725000261 Published online by Cambridge University Press

these patterns, we note that the axial ratio remains below 6 dB throughout the entire upper region of all four plots. The excellent agreement between experimental and theoretical results validates the proposed model and confirms the effectiveness of the design strategy.

To clarify the principle of circular polarization reconfiguration, fig. 7 shows the magnitude of the electric field inside the dielectric substrate for both configurations mentioned. The analysis encompasses four consecutive excitation phases (0°, 45°, 90°, and 135°). fig. 7(a) demonstrates the anticlockwise field rotation (antenna top view), with the main beam propagating out of the page along the z-direction, leading to RHCP polarization. On the other hand, fig. 7(b) presents the field distribution for LHCP operation, showcasing the reverse rotation.

Before concluding this section, it is important to note that the bias voltages applied to the varicap diodes can be adjusted to tune the frequency of the minimum broadside axial ratio around 1.575 GHz. This feature allows the antenna to reconfigure its frequency for small ratios. Most polarization-reconfigurable antennas use p-i-n diodes to switch between polarization states [30], which often require complex circuitry to achieve frequency reconfiguration, even for small variations, or cannot incorporate frequency reconfiguration at all [31, 32]. Therefore, the proposed antenna is well-suited for narrow band applications that need polarization reconfiguration between RHCP and LHCP states, as well as frequency tuning.

Conclusion

This letter introduces an improved analytical model for analyzing microstrip antennas loaded by metallic vias terminated with lumped loads. The proposed formulation addresses the procedure for computing the radiated fields, including all modes supported by the equivalent cavity. The model was applied to both CP and LP radiators, and the results compare well with those from HFSS. Additionally, a prototype of a polarization-reconfigurable antenna was designed based on the values obtained from the model. Only a slight adjustment in the bias voltages of the varicaps relative to the theoretical values was necessary to achieve a low-measured AR, demonstrating that the model is a powerful tool for predesign, in addition to offering valuable physical insights into the antenna operation. Furthermore, it can be readily extended to other microstrip antenna geometries, such as cylindrical, spherical, conical, and even circular patches.

Acknowledgement. This work was supported by the National Council for Scientific and Technological Development – CNPq – Brazil (Grants: 405889/2021-6 and 305944/2023-1).

Competing interest. None declared.

References

1. **Schaubert D, Farrar F, Sindoris A and Hayes S** (1981) Microstrip antennas with frequency agility and polarization diversity. *IEEE Transactions on Antennas and Propagation* **29**(1), 118–123.
2. **Richards W and Long S** (1986) Reactively loaded microstrip antennas. *IEEE Antennas and Propagation Society Newsletter* **28**(5), 10–17.
3. **Liu Z, He Y and Li Y** (2023) Beamwidth enhancement of microstrip antennas using capacitive via-fence loading. *IEEE Open Journal of Antennas and Propagation* **4**, 151–158.
4. **Nguyen-Trong N, Hall L and Fumeaux C** (2016) A frequency- and pattern-reconfigurable center-shorted microstrip antenna. *IEEE Antennas and Wireless Propagation Letters* **15**, 1955–1958.
5. **Han S, Wang Z and Dong Y** (2024) Miniaturized circularly polarized reconfigurable capacitance-loaded patch antenna. *IEEE Antennas and Wireless Propagation Letters* **23**(4), 1226–1230.
6. **Gao GP, Zhang BK, Dong JH, Dou ZH, Yu ZQ and Hu B** (2023) A compact dual-mode pattern-reconfigurable wearable antenna for the 2.4-GHz WBAN application. *IEEE Transactions on Antennas and Propagation* **71**(2), 1901–1906.
7. **Qin P-Y, Wei F and Guo YJ** (2015) A wideband to narrowband tunable antenna using a reconfigurable filter. *IEEE Transactions on Antennas and Propagation* **63**(5), 2282–2285.
8. **Chen S-L, Wei F, Qin P-Y, Guo YJ and Chen X** (2017) A multilinear polarization reconfigurable unidirectional patch antenna. *IEEE Transactions on Antennas and Propagation* **65**(8), 4299–4304.
9. **Nunes R, Moleiro A, Rosa J and Peixeiro C** Dual-band microstrip patch antenna element with shorting pins for GSM. In *IEEE Antennas and Propagation Society International Symposium. Transmitting Waves of Progress to the Next Millennium. 2000 Digest. Held in conjunction with: USNC/URSI National Radio Science Meeting (C*, 16–21 July 2000. 4, 2208–2211, doi: 10.1109/APS.2000.874932
10. **Fong LK and Chair R** (2004) On the use of shorting pins in the design of microstrip patch antennas. *HKIE Transactions* **11**(4), 31–38.
11. **Liu ZX, Zhu L and Liu NW** (2020) Design approach for compact dual-band dual-mode patch antenna with flexible frequency ratio. *IEEE Transactions on Antennas and Propagation* **68**(8), 6401–6406.
12. **Huang C, Guo C, Li W, Xu J and Ding J** (2022) Novel method for reshaping TM00 mode radiation patterns of rectangular patch antenna by using characteristic mode analysis. *International Journal of RF and Microwave Computer-Aided Engineering* **32**(10), e23311.
13. **Tang SC, Wang XY, Yu W, Yang WW and Chen JX** (2023) Compact microstrip patch filtenna array based on reusable high-order SIW cavity. *IEEE Antennas and Wireless Propagation Letters* **22**(2), 268–272.
14. **Cai S, Liu J and Long Y** (2020) Investigation of SIW cavity-backed slot and patch antennas with conical radiation patterns. *IEEE Transactions on Antennas and Propagation* **68**(8), 5978–5988.
15. **Dos Santos Silveira E, Antreich F and Do Nascimento DC** (2020) Frequency-reconfigurable SIW microstrip antenna. *AEU - International Journal of Electronics and Communications* **124**, 153333.
16. **Chapari A, Zeidaabadi Nezhad A and Firouzeh ZH** (2017) Analytical approach for compact shorting pin circular patch antenna. *IET Microwaves, Antennas & Propagation* **11**(11), 1603–1608.
17. **Richards WF and Lo YT** (1983) Theoretical and experimental investigation of a microstrip radiator with multiple lumped linear loads. *Electromagnetics* **3**(3-4), 371–385.
18. **Richards W, Davidson S and Long S** (1985) Dual-band reactively loaded microstrip antenna. *IEEE Transactions on Antennas and Propagation* **33**(5), 556–561.
19. **Sung Y** (2010) A novel reconfigurable microstrip antenna with polarization diversity. *Microwave and Optical Technology Letters* **52**(9), 2053–2056.
20. **Pyo S and Shin I** (2012) A miniaturized switchable circularly polarized patch antenna controlled by a single diode operation. *Microwave and Optical Technology Letters* **54**(10), 2375–2378.
21. **Hammerstad EO** Equations for microstrip circuit design. in *1975 5th European Microwave Conference*, 1–4 September 1975. 268–272, doi: 10.1109/EUMA.1975.332206
22. **Richards W, Yuen L and Harrison D** (1981) An improved theory for microstrip antennas and applications. *IEEE Transactions on Antennas and Propagation* **29**(1), 38–46.
23. **R. Garg, I. Bahl** Ed (1986) *Microstrip Antenna Design Handbook*. Norwood, MA: Artech House.
24. **Lo Y, Solomon D and Richards W** (1979) Theory and experiment on microstrip antennas. *IEEE Transactions on Antennas and Propagation* **27**(2), 137–145.
25. **Lumini F, Cividanes L and da S. Lacava JC** (1999) Computer aided design algorithm for singly fed circularly polarized rectangular microstrip patch

https://doi.org/10.1017/S1759078725000261 Published online by Cambridge University Press

antennas. *International Journal of RF and Microwave Computer-Aided Engineering* **9**(1), 32–41.
26. **J. R. James, C. Wood** Ed (1981) *Microstrip Antenna Theory and Design*. London, United Kingdom: Peter Peregrinus Ltd.
27. **Balanis CA** (1989) *Advanced Engineering Electromagnetics*. Hoboken: John Wiley & Sons.
28. **Asgarimehr M, Hoseini M, Semmling M, Ramatschi M, Camps A, Nahavandchi H, Hass R and Wickert J** (2022) Remote sensing of precipitation using reflected GNSS signals: Response analysis of polarimetric observations. *IEEE Transactions on Geoscience and Remote Sensing* **60**, 1–12.
29. **Sirci S, Martínez JD, Taroncher M and Boria VE** Varactor-loaded continuously tunable SIW resonator for reconfigurable filter design. in *2011 41st European Microwave Conference*, 10–13 October 2011. 436–439, doi: 10.23919/EuMC.2011.6101994
30. **Alhamad R, Almajali E and Mahmoud S** (2023) Electrical reconfigurability in modern 4G, 4G/5G and 5G antennas: A critical review of polarization and frequency reconfigurable designs. *IEEE Access* **11**, 29215–29233.
31. **Al-Yasir YIA, Abdullah AS, Parchin NO, Abd-Alhameed RA and Noras JM** (2018) A new polarization-reconfigurable antenna for 5G applications. *Electronics* **7**, 1–9.
32. **Row J-S and Hou M-J** (2014) Design of polarization diversity patch antenna based on a compact reconfigurable feeding network.*IEEE Transactions on Antennas and Propagation* **62**(10), 5349–5352.



Fúlvio F. Oliveira received his B.S. degree in telecommunications engineering from the Instituto Nacional de Telecomunicações (INATEL), in 2006, and his M.S. degree in electronic engineering from the Aeronautics Institute of Technology (ITA), S. J. dos Campos, Brazil, in 2021. He is currently manager of the Weapon Systems of the Brazil's Navy. His research interests include microwave engineering, electromagnetic theory, and antennas.



Juner M. Vieira received his B.S. in Telecommunications Engineering from the Federal University of Pampa in 2017, his M.S. in Electrical Engineering from the same institution in 2019, and his Ph.D. in Electronics Engineering focusing on microwave and antennas from the Aeronautics Institute of Technology in 2023. He is currently a Technological Development fellowships holder within the Space Electronics and Computing Division at INPE (Brazil). His research interests include microwave circuits, microstrip antennas, and antenna arrays.



Daniel B. Ferreira received the B.S. degree (*summa cum laude*) in electronics engineering and the M.S. and D.S. degrees in electronics and computer engineering from the Aeronautics Institute of Technology, Sao Jose dos Campos, Brazil, in 2009, 2011, and 2017, respectively. He is currently an Assistant Professor at the Department of Microwaves and Optoelectronics, Aeronautics Institute of Technology, Sao Jose dos Campos, Brazil, and a member of the Laboratory of Antennas and Propagation (LAP/ITA). His research work is mainly focused on microstrip antennas mounted on curved surfaces, frequency-independent antennas, and antenna arrays.



Daniel C. Nascimento received his B.S. degree in telecommunication engineering from the University of Taubaté, Taubaté, Brazil, in 2004, and the M.S. and Ph.D. degrees in electronic engineering from the Aeronautics Institute of Technology (ITA), São José dos Campos, Brazil, in 2007 and 2013, respectively. In 2009, he was appointed as an Assistant Professor with the Department of Electronic Engineering, ITA, where he has been an Associate Professor since 2021. He is currently the Head of the Laboratory of Antennas and Propagation, ITA. His research interests include the areas of microstrip antennas, phased arrays, and direction-finding systems.

https://doi.org/10.1017/S1759078725000261 Published online by Cambridge University Press